IJMMM International Journal of Minerals, Metallurgy and Materials 矿物冶金与材料学报（英文版）

TiO_2@NH_2-MIL-125(Ti) composite derived from a partial-etching strategy with enhanced carriers' transfer for the rapid photocatalytic Cr(VI) reduction

Fang Xu, Wanning Cao, Jinzhou Li, Songsong Zhi, Zhiyong Gao, Yuqin Jiang, Wei Li, Kai Jiang, and Dapeng Wu

Cite this article as:
Fang Xu, Wanning Cao, Jinzhou Li, Songsong Zhi, Zhiyong Gao, Yuqin Jiang, Wei Li, Kai Jiang, and Dapeng Wu, TiO_2@NH_2-MIL-125(Ti) composite derived from a partial-etching strategy with enhanced carriers' transfer for the rapid photocatalytic Cr(VI) reduction, *Int. J. Miner. Metall. Mater.*, 30(2023), No. 4, pp. 630-641. https://doi.org/10.1007/s12613-022-2559-4

View the article online at SpringerLink or IJMMM Webpage.

Articles you may be interested in

Xiong-feng Zeng, Jian-sheng Wang, Ying-na Zhao, Wen-li Zhang, and Meng-huan Wang, Construction of TiO_2-pillared multilayer graphene nanocomposites as efficient photocatalysts for ciprofloxacin degradation, *Int. J. Miner. Metall. Mater.*, 28(2021), No. 3, pp. 503-510. https://doi.org/10.1007/s12613-020-2193-y

Lalinda Palliyaguru, Ushan S. Kulathunga, Lakruwani I. Jayarathna, Champa D. Jayaweera, and Pradeep M. Jayaweera, A simple and novel synthetic route to prepare anatase TiO_2 nanopowders from natural ilmenite via the H_3PO_4/NH_3 process, *Int. J. Miner. Metall. Mater.*, 27(2020), No. 6, pp. 846-855. https://doi.org/10.1007/s12613-020-2030-3

Cheng-bin Shi, Ding-li Zheng, Seung-ho Shin, Jing Li, and Jung-wook Cho, Effect of TiO_2 on the viscosity and structure of low-fluoride slag used for electroslag remelting of Ti-containing steels, *Int. J. Miner. Metall. Mater.*, 24(2017), No. 1, pp. 18-24. https://doi.org/10.1007/s12613-017-1374-9

Jing Zhou, Dan-dan Nie, Xian-bo Jin, and Wei Xiao, Controllable nitridation of Ta_2O_5 in molten salts for enhanced photocatalysis, *Int. J. Miner. Metall. Mater.*, 27(2020), No. 12, pp. 1703-1710. https://doi.org/10.1007/s12613-020-2050-z

Yan-xiang Liu, Jian-liang Zhang, Zhi-yu Wang, Ke-xin Jiao, Guo-hua Zhang, and Kuo-chih Chou, Dripping and evolution behavior of primary slag bearing TiO_2 through the coke packed bed in a blast-furnace hearth, *Int. J. Miner. Metall. Mater.*, 24(2017), No. 2, pp. 130-138. https://doi.org/10.1007/s12613-017-1387-4

Hai-xia Liu, Meng-yuan Teng, Xu-guang Wei, Tian-duo Li, Zai-yong Jiang, Qing-fen Niu, and Xu-ping Wang, Mosaic structure ZnO formed by secondary crystallization with enhanced photocatalytic performance, *Int. J. Miner. Metall. Mater.*, 28(2021), No. 3, pp. 495-502. https://doi.org/10.1007/s12613-020-2033-0

IJMMM WeChat

QQ author group

International Journal of Minerals, Metallurgy and Materials
Volume 30, Number 4, April 2023, Page 630
https://doi.org/10.1007/s12613-022-2559-4

TiO_2@NH_2-MIL-125(Ti) composite derived from a partial-etching strategy with enhanced carriers' transfer for the rapid photocatalytic Cr(VI) reduction

Fang Xu[1)], *Wanning Cao*[1)], *Jinzhou Li*[1)], *Songsong Zhi*[2)], *Zhiyong Gao*[1)], *Yuqin Jiang*[1),✉], *Wei Li*[1)], *Kai Jiang*[2)], *and Dapeng Wu*[2),✉]

1) Collaborative Innovation Center of Henan Province for Green Manufacturing of Fine Chemicals, Key Laboratory of Green Chemical Media and Reactions, Ministry of Education, School of Chemistry and Chemical Engineering, Henan Normal University, Xinxiang 453007, China
2) School of Environment, Henan Normal University, Xinxiang 453007, China
(Received: 28 July 2022; revised: 26 September 2022; accepted: 4 October 2022)

Abstract: Metal-organic frameworks (MOFs)-based composites have been widely applied as photocatalysts because of their synergistic effect between the two individual component. Herein, TiO_2@NH_2-MIL-125(Ti) nanocomposites which possess unsaturated titanium–oxo clusters, mesoporous structure, and intimate interface were successfully constructed via an *in-situ* distilled water-etched route. The X-ray photoelectron spectroscopy (XPS) measurements indicated strong electronic interaction between TiO_2 and NH_2-MIL-125(Ti), confirming the formation of TiO_2@NH_2-MIL-125(Ti) nanocomposite. Photoelectrochemical and thermodynamics measurements showed that TiO_2@NH_2-MIL-125(Ti) nanocomposites have improved charge separation efficient and decreased transfer resistance of the carriers within the heterojunction interfaces, which facilitates the photoexcited electrons transfer and reduction of the Cr(VI) species. Therefore, the optimal TiO_2@NH_2-MIL-125(Ti) nanocomposite demonstrated superior performance compared to NH_2-MIL-125(Ti) and NH_2-MIL-125(Ti) derived TiO_2. Based on the free radical trapping experiment and electron paramagnetic resonance (EPR) measurements, a possible type-II scheme was proposed for the enhanced photocatalytic activity over the TiO_2@NH_2-MIL-125(Ti) nanocomposite.

Keywords: NH_2-MIL-125; titanium dioxide; distilled water-etched route; photocatalysis; hexavalent chromium reduction

1. Introduction

Hexavalent chromium (Cr(VI)) as a common industrial heavy metal pollutant is highly toxic to aquatic organisms and humans on account of its good water solubility and high carcinogenicity [1–2]. Compared with Cr(VI), Cr(III) is more than 100 times less toxic and can form $Cr(OH)_3$ precipitation easily under alkaline conditions. Therefore, the universal treatment for chromium-containing waste water is the reduction of Cr(VI) to Cr(III). Among different kinds of methods [3–6], photocatalytic reduction of Cr(VI) into Cr(III) has been regarded as an effective and energy-saving route [7–10].

Recently, metal-organic frameworks (MOFs) which has high porosity, large surface area, highly-ordered crystallinity, and structural and functional tailorability have been widely applied as photocatalysts [11–19]. Among various MOFs, MIL-125(Ti) and its derivatives have attracted extensive and constant attentions because of the low toxicity and unique photocatalytic properties of Ti element [20–23]. Particularly, amino-functionalized MIL-125(Ti) (NH_2-MIL-125(Ti)) can extend photoresponse range from UV to visible light, which is significant for improving light absorption capacity of photocatalysts [24–32]. Also, the small radius of Ti^{4+} endows it strong Ti–O bonding, and the reversible redox transition between Ti^{4+}/Ti^{3+} under photo-excitation enables the Ti-based MOFs to store charge effectively. Although NH_2-MIL-125(Ti) has numerous promising advantages as a photocatalyst, it also suffers from certain disadvantages, such as hindered mass transport through micropores, high recombination tendency of photogenerated carriers, etc., which severely limit the photocatalytic performance. To overcome these limitations and further improve the total photocatalytic performance, diverse strategies, including pyrolysis of MOF into different functional materials [33–34], formation of heterojunctions [35–37], etc., have been employed.

TiO_2 is a widely accepted photocatalyst owing to its advantageous properties of low toxicity, biocompatibility, chemical stability, and low cost [38–42]. However, the photocatalytic efficiency of TiO_2 is severely inhibited because of its wide bandgap. Therefore, some strategies, such as doping [43–44], forming heterojunction [45–46], co-cocatalyst coupling [47], etc., have been developed to improve the pho-

✉ Corresponding authors: Yuqin Jiang E-mail: jiangyuqin@htu.cn; Dapeng Wu E-mail: dapengwu@htu.edu.cn
© University of Science and Technology Beijing 2023

tocatalytic performance. It is important to mention that, the conduction band minimum (CBM) and valence band maximum (VBM) of TiO_2 match well with the lowest unoccupied molecular orbital (LUMO) and highest occupied molecular orbital (HOMO) of NH_2-MIL-125(Ti) for Type-II heterojunction. Thus, TiO_2@NH_2-MIL-125(Ti) nanocomposites have been widely synthesized such as hydrolysis of tetrabutyl titanate [48–49] for photocatalytic application. It is worth mentioning that the controllable loss of organic ligand and maintaining the intrinsic advantages of MOF at the same time are important for achieving TiO_2@NH_2-MIL-125(Ti) with desirable composition, structures, interface, and photocatalytic performance. For example, "post-solvothermal route" [50–51] and *in situ* acid-etched strategy [52–53] using NH_2-MIL-125(Ti) as precursor have been reported for controllable synthesis of TiO_2/NH_2-MIL-125(Ti) nanocomposites. However, *in situ* synthesis of TiO_2@NH_2-MIL-125(Ti) nanocomposites using distilled water as etchant is environmental friendly and has been scarcely reported.

In this study, we propose a distilled water-etched route for the synthesis of TiO_2@NH_2-MIL-125(Ti) nanocomposite using NH_2-MIL-125(Ti) as precursor. During the etching process, NH_2-MIL-125(Ti) can be transformed into TiO_2@NH_2-MIL-125(Ti) nanocomposite by partly destroying the organic ligand, and keeping many linker defects and producing mesoporous structures simultaneously. TiO_2@NH_2-MIL-125(Ti) nanocomposite exhibited improved photocatalytic performance in Cr(VI) reduction reaction compared with NH_2-MIL-125(Ti) and NH_2-MIL-125(Ti)-derived TiO_2 under the irradiation of 300 W Xe lamp. The cycling experiments confirmed its good stability and reusability. The synthesis and further application of TiO_2@NH_2-MIL-125(Ti) nanocomposite are illustrated in Fig. 1.

2. Experimental

2.1. Preparation of NH_2-MIL-125(Ti)

NH_2-MIL-125(Ti) was prepared using tetrabutyl titanate (TBT) as Ti salt and 2-amino terephthalic acid as organic liner as reported previously [54]. The typical procedure is as following. First, 28 mL of N,N-dimethylformamide (DMF) and 3 mL of methyl alcohol were well mixed under magnetic stirring. Then, 1.62 g of 2-amino terephthalic acid and 0.85 mL of TBT were dropped into the mixed solvent under continuous magnetic stirring. Finally, the suspension was transferred into a 50 mL Teflon-lined autoclave and heated at 160°C for 24 h. After naturally cooling down to room temperature, the sample was collected by centrifugation, thoroughly washed with methyl alcohol and DMF for 3–5 times, and dried overnight at 60°C.

2.2. Preparation of TiO_2@NH_2-MIL-125(Ti) nanocomposite

Firstly, the as-prepared NH_2-MIL-125(Ti) (0.12 g) was dispersed into 10 mL of alcohol, and then distilled water was dropped into the dispersion under magnetic stirring. After that, the suspension was transferred into a 25 mL Teflon-lined autoclave and heated at 200°C for 2 h. After naturally cooling down to room temperature, the sample was collected by centrifugation, thoroughly washed with alcohol 3–5 times, and dried overnight at 60°C. For comparison, the amount of distilled water was settled as 0.5, 1, 2, and 5 mL, and the corresponding samples were marked as MT-0.5, MT-1, MT-2, and TiO_2. The pure NH_2-MIL-125(Ti) was marked as M.

2.3. Photocatalytic performance tests

The photocatalytic reduction of Cr(VI) was performed under the irradiation of a 300 W Xe lamp at ~20°C using a water bath cooling system. The optical spectrum and the intensity of incident light are shown in Fig. S1(a). The photocatalytic performance of MT-2 was also measured under the irradiation of 300 W Xe lamp with band-pass filters with central wavelengths of 365, 400, and 500 nm (the parameters are shown in Table S1). The transmissions of band-pass filters with central wavelengths of 365, 400, and 500 nm are shown in Fig. S1(b)–(d). Aqueous Cr(VI) with a concentration of 5 mg/L was prepared by dissolving $K_2Cr_2O_7$ in distilled water. Typically, 20 mg photocatalyst was dispersed in 50 mL of Cr(VI) aqueous solution in a quartz glass reactor and the suspension was stirred continuously in dark for 60 min to reach adsorption/desorption equilibrium. Then, the light was turned on to stimulate photocatalytic reaction. 1.5 mL of the

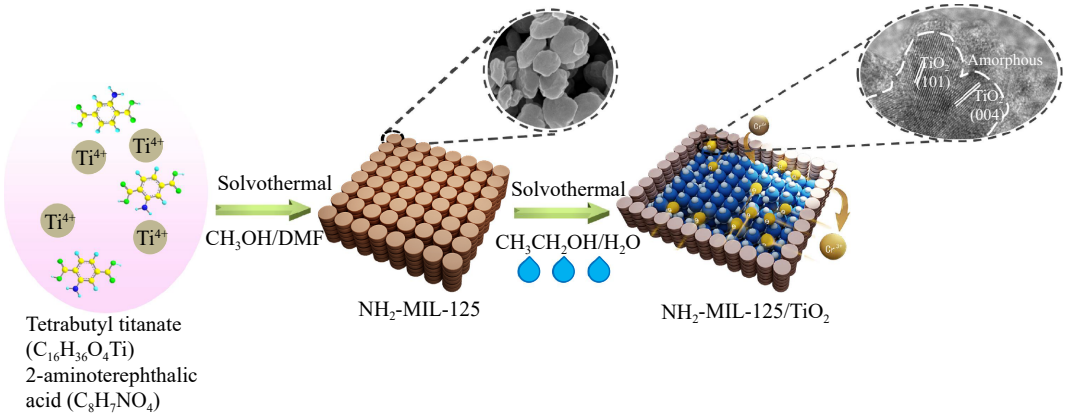

Fig. 1. Schematic illustration for the preparation of TiO_2@NH_2-MIL-125(Ti) nanocomposites and application for photocatalytic Cr(VI) reduction.

suspension was collected at given time intervals and filtered using a 0.22-μm poly tetra fluoroethylene (PTFE) microporous membrane and the supernatant was used to determine the residual Cr(VI) concentration by the diphenylcarbazide colorimetric method on a UV–Vis spectrophotometer. The stability and usability of the photocatalyst were studied by a cycling test. That is, after each photocatalytic reduction Cr(VI) experiment completed, the photocatalyst was separated from the suspension, and then used for the next photocatalytic reaction under the same conditions.

Also, we performed photocatalytic degradation of methylene blue (MB) under the irradiation of a 300 W Xe lamp at ~20°C using a water bath cooling system. Typically, 10 mg TiO_2@NH_2-MIL-125(Ti) composite was dispersed into 50 mL MB solution (20 mg/L) and kept stirring in dark for 1 h to reach adsoprtion–desorption equilibrium. Then, ~1.5 mL of the suspension was collected for 1 h and filtered using a 0.22-μm PTFE microporous membrane and the supernatant was used to determine the residual MB concentration on a UV–Vis spectrophotometer.

3. Results and discussion

3.1. Structure, composition and morphology characterization

The morphology and composition of TiO_2@NH_2-MIL-125(Ti) nanocomposite were investigated by scanning electron microscopy (SEM) and transmission electron microscopy (TEM) measurements taking MT-2 as an example. The SEM image of NH_2-MIL-125(Ti) (Fig. 2(a)) revealed the disc-like particles with an average diameter of ~200 nm. The SEM image of MT-2 (Fig. 2(b)) exhibited nanoparticles with a diameter of ~20 nm, indicating the transformation from disc-like NH_2-MIL-125(Ti) into small nanoparticles for TiO_2@NH_2-MIL-125(Ti) nanocomposite. The diameter distribution histogram of MT-2 calculated based on Fig. 2(b) is shown in Fig. S2, and the average diameter of MT-2 was 25.26 nm. The TEM image of MT-2 (Fig. 2(c)) also showed small nanoparticles of MT-2, which further confirmed the destruction of the crystal structure of NH_2-MIL-125(Ti). Moreover, the high-resolution transmission electron microscopy (HRTEM) (Fig. 2(d)) of MT-2 revealed that the spacings of lattice fringes were ~0.352 nm and ~0.237 nm, which correspond to (101) and (004) planes of anatase TiO_2. Also, some poor crystallized zone can be detected as highlighted in the white cycles, which is the reserved NH_2-MIL-125(Ti). The high-angle annular dark field TEM (HAADF-TEM) images (Fig. 2(e)) and the corresponding dispersive X-ray mapping images demonstrated the distribution of Ti, O, C, and N elements in MT-2.

The X-ray diffraction (XRD) patterns of as-prepared samples are shown in Fig. 3(a). The characteristic peaks of NH_2-MIL-125(Ti) (M) demonstrated similar patterns to those reported by Nasalevich *et al.* [55]. After the post-treatment by distilled water, new peaks appeared and became stronger with increasing distilled water amount from 0.5 to 5 mL. Concomitantly, the diffraction peaks of NH_2-MIL-125(Ti) became weaker and disappeared when the amount of distilled water reached 5 mL. The new diffraction peaks located at 25.3°, 37.9°, 48.0°, 54.3°, 63.2°, and 75.1° could be assigned to (101), (004), (200), (105), (204), and (215) lattice planes of anatase TiO_2 (PDF: 99-0008) [56]. The results indicated that the post-treatment by introducing appropriate amount of distilled water could destroy the NH_2-MIL-125(Ti) crystal structure and generate TiO_2@NH_2-MIL-125(Ti) nanocomposite simultaneously. Notably, when the distilled water amount reached 5 mL, NH_2-MIL-125(Ti) converted into anatase phase of TiO_2 completely.

The functional groups and molecular structure of as-prepared samples were measured by Fourier transform infrared

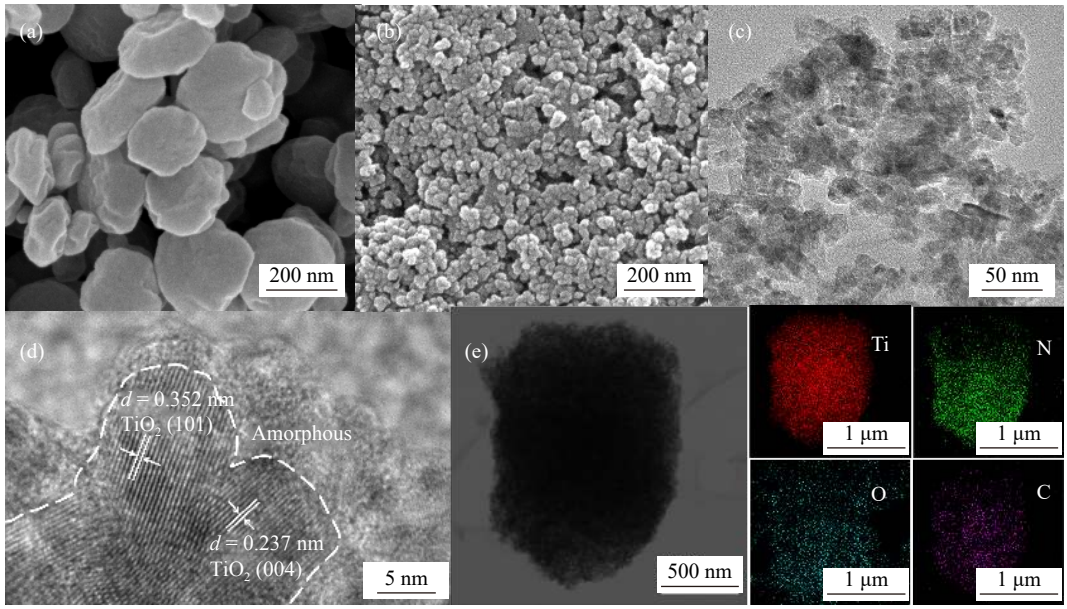

Fig. 2. SEM images of (a) NH_2-MIL-125(Ti) and (b) MT-2; (c) TEM and (d) HRTEM images of MT-2; (e) HAADF-TEM image and the corresponding elemental mapping of MT-2.

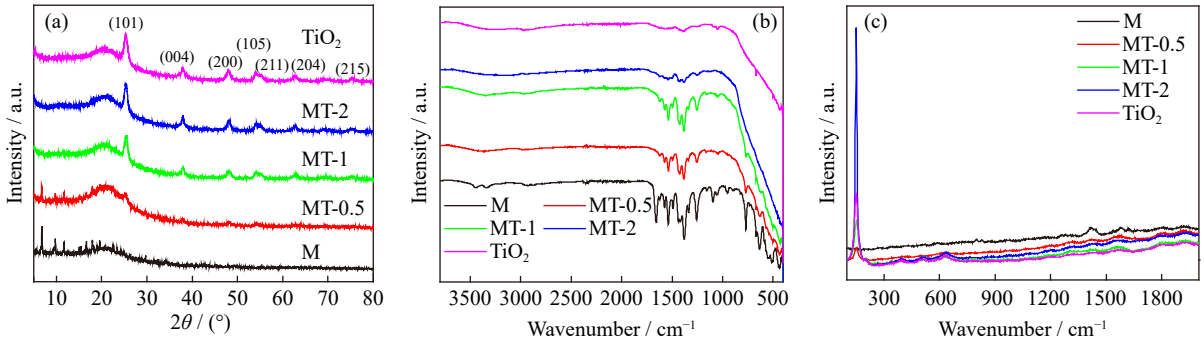

Fig. 3. (a) XRD pattern, (b) FTIR spectra, and (c) Raman spectra of NH_2-MIL-125(Ti), TiO_2@NH_2-MIL-125, and NH_2-MIL-125 derived TiO_2.

spectroscopy (FTIR) spectroscopy and are shown in Fig. 3 (b). The characteristic bands in the range of 400–800 cm^{-1} can be ascribed to the Ti–O–Ti stretching vibrations; the bands at ~3345 and ~3440 cm^{-1} correspond to the symmetric and asymmetric stretching vibrations of amines; the peaks at ~1255 and ~1654 cm^{-1} are assigned to the C–N stretching and N–H bending vibrations, respectively; the peaks at ~1431 and ~1531 cm^{-1} correspond to the carbonyl symmetric stretching vibration [57]. Furthermore, when the amount of distilled water increased from 0.5 to 2 mL, the typical peaks of NH_2-MIL-125(Ti) became weaker and further disappeared as the amount of distilled water reached 5 mL. The results confirmed that the structure of NH_2-MIL-125(Ti) was degraded due to the adding of distilled water and further converted to TiO_2 completely. The Raman spectra shown in Fig. 3(c) exhibited four Raman active fundamental modes, including one strong band at 154 cm^{-1} and three weak ones at 398, 515, and 637 cm^{-1}, which are assigned to e_g, b_{1g}, b_{1g} + a_{1g}, and e_g, respectively, confirming the existence of anatase TiO_2 [58]. In contrast, no Raman shift can be observed in the spectrum of M.

The surface composition and structure of TiO_2@NH_2-MIL-125(Ti) were analyzed using MT-2 as an example via X-ray photoelectron spectroscopy (XPS) measurements. In the XPS survey spectrum of M and MT-2 (Fig. S3), the peaks of O 1s, Ti 2p, C 1s, and N 1s can be found, which suggested that there are O, Ti, C, and N elements in MT and MT-2. In addition, the peak intensities of C 1s and N 1s weakened and those of Ti 2p strengthened for MT-2 compared with M. In the high resolution XPS spectrum of Ti 2p (Fig. 4(a)), two peaks centered at ~458.8 and ~464.6 eV in NH_2-MIL-125(Ti) correspond to Ti $2p_{1/2}$ and Ti $2p_{3/2}$ respectively, confirming the presence of Ti^{4+} in the titanium–oxo cluster. Moreover, the binding energies of Ti shifted to lower binding energies of ~458.4 and ~464.1 eV for MT-2, revealing the generation of Ti^{3+} and linker defects in TiO_2@NH_2-MIL-125(Ti). In addition, the formation of Ti^{3+} was further proved via electron paramagnetic resonance (EPR) spectroscopy (Fig. S4). As indicated in Fig. S4, no paramagnetic signals could be detected for NH_2-MIL-125 due to the $3d^0$ electronic configuration of Ti^{4+}. However, a strong paramagnetic signal at a *g*-value of 1.9996 appeared for the TiO_2@NH_2-MIL-125(Ti) (MT-2), confirming the existence of Ti^{3+} [59]. For the high resolution XPS spectrum of N 1s (Fig. 4(b)), two main peaks at binding energies of 399.5 and 402.9 eV for M correspond to the N in $–NH_2$ and the positively charged nitrogen of the $–N=^+$ and $–NH–^+$, respectively. For MT-2, the binding energy of N 1s shifted to lower energy compared with NH_2-MIL-125(Ti). In the high resolution XPS spectrum of O 1s (Fig. 4(c)), the characteristic peaks of NH_2-MIL-125 centered at ~530.4 and ~531.8 eV are attributed to the lattice oxygen of titanium–oxo cluster and C–O in organic 1,4-benzenedicarboxylate (BDC) linkers respectively. The binding energy of O 1s for MT-2 shifted to higher binding energies of ~530.6 and ~532.1 eV compared with NH_2-MIL-125, suggesting the electron transfer from the surface oxygen in TiO_2 to the $–NH–^+$ in MT-2. The binding energies at 532.5 and 532.75 eV for M and MT-2 are attributed to the adsorbed hydroxy. The C 1s XPS spectrum of NH_2-MIL-125 could be fitted into three peaks (Fig. 4(d)), which are ascribed to C–C (284.5 eV), C–O (286.5 eV), C=O (288.7 eV), and C–N (285.0 eV) of NH_2-MIL-125, respectively. For MT-2, the binding energies for C–O (286.3 eV) and C=O (288.6 eV) slightly shifted to lower energies compared with NH_2-MIL-125. The results proved the strong electronic interaction between TiO_2 and NH_2-MIL-125(Ti) for TiO_2@NH_2-MIL-125 composite.

Further, we attempted to determine the ratios of TiO_2 and NH_2-MIL-125(Ti) in TiO_2@NH_2-MIL-125(Ti) through XPS data semi-quantitatively. The peak area and atomic percentages of O, Ti, C, N elements in M and MT-2 are shown in Table S2. The atomic percentages of O and Ti increased from 29.2% and 8.81% for M to 49.35% and 22.21% for MT-2. At the same time, the atomic percentages of C and N decreased from 56.49% and 5.5% for M to 25.61% and 2.83% for MT-2. The increased atomic percentages of Ti and O are resulted from the formation of TiO_2. The mole ratios of TiO_2 and NH_2-MIL-125(Ti) in MT-2 can deduced from the atomic percentages to be ~91% and 8%, respectively.

The N_2 adsorption–desorption isotherm of the NH_2-MIL-125(Ti), TiO_2@NH_2-MIL-125 nanocomposites, and NH_2-MIL-125 derived TiO_2 was measured to evaluate the specific surface area and porous structure. As shown in Fig. 5(a), the type-I isotherm for pristine NH_2-MIL-125(Ti) (M) indicated the microporous structures. For MT-0.5, MT-1, and MT-2, a hysteresis loop appeared and gradually widened, suggesting the type-IV isotherm for TiO_2@NH_2-MIL-125 nanocomposites and the mesoporous features. The calculated Brunauer-Emmett-Teller (BET) surface areas shown in Table S3 were

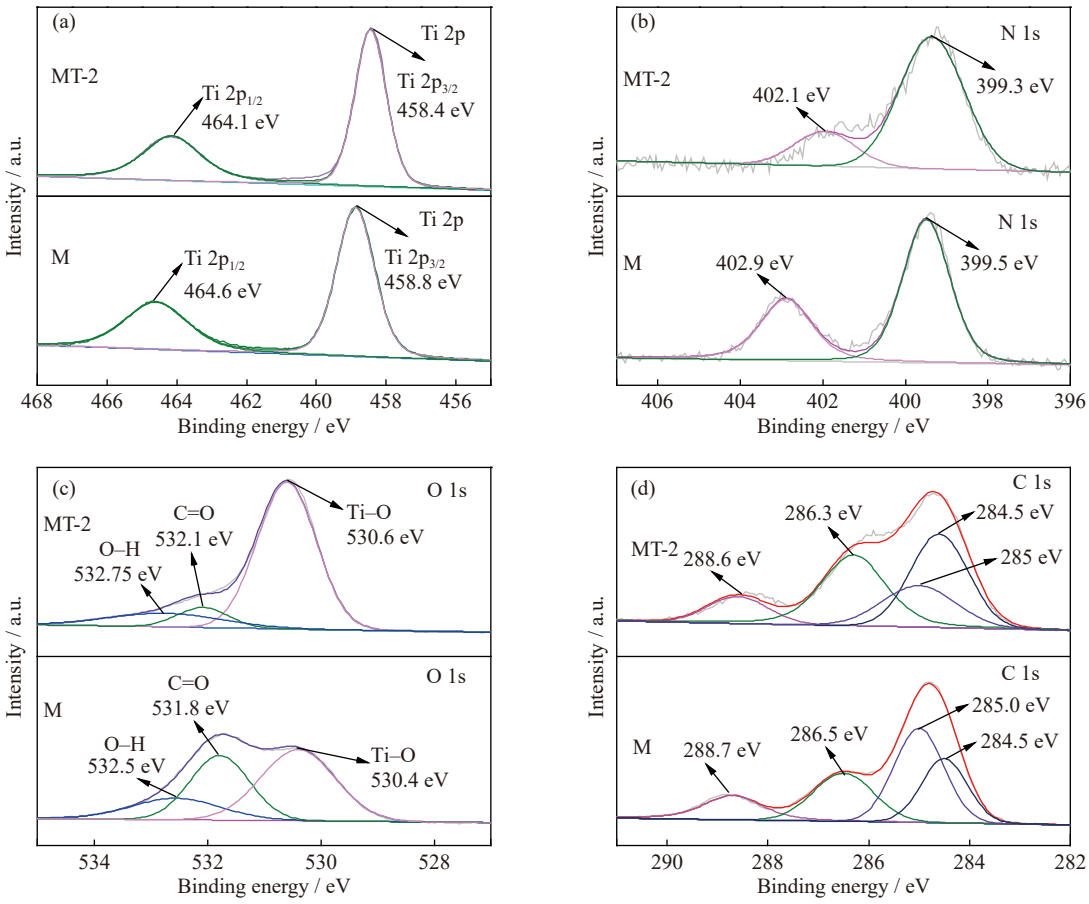

Fig. 4. High resolution XPS spectra of (a) Ti 2p, (b) N 1s, (c) O 1s, and (d) C 1s for M and MT-2.

1210.45 m^2/g (M), 463.45 m^2/g (MT-0.5), 347.25 m^2/g (MT-1), and 105.28 m^2/g (MT-2). The corresponding pore volumes were calculated to be 0.61, 0.56, 0.53, and 0.47 $cm^3/(g \cdot nm)$. The corresponding pore size distribution shown in Fig. 5 also proved the microporous characteristics for M and the mesoporous characteristics for TiO_2@NH_2-MIL-125(Ti) nanocomposites. The conversion of microporous structure for NH_2-MIL-125(Ti) to the mesoporous structure for TiO_2@NH_2-MIL-125(Ti) nanocomposites and the significantly decreased BET surface areas are resulted from the ligand loss after the post-treatment by distilled water. For NH_2-MIL-125(Ti) derived TiO_2, a larger specific surface (117.44 m^2/g) and a smaller pore volume were observed compared with MT-2, which are resulted from the complete

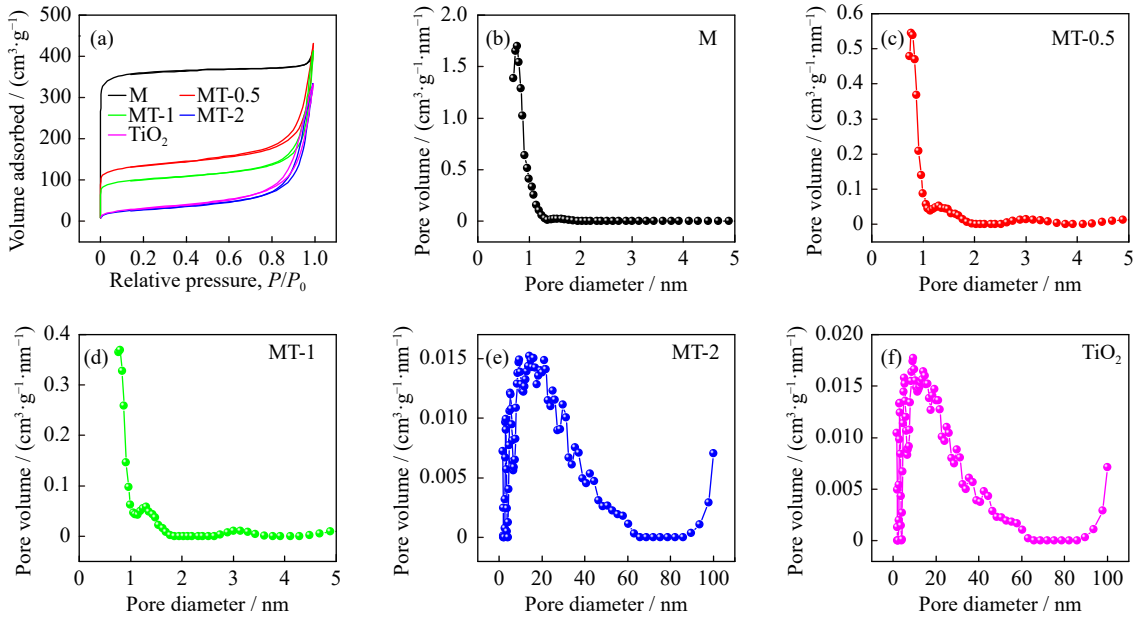

Fig. 5. (a) N_2 absorption–desorption isotherm and (b–f) pore size distributions of NH_2-MIL-125, TiO_2@NH_2-MIL-125, and TiO_2.

loss of organic ligand and the TiO_2 preserved porous structure of NH_2-MIL-125(Ti).

3.2. Optical response and electronic structure characterization

In order to elucidate the light absorption of TiO_2@NH_2-MIL-125(Ti) nanocomposites, UV–Vis diffuse reflectance spectroscopy (DRS) was analyzed (Fig. 6(a)). As indicated in the UV–Vis spectrum of M, the adsorption band edges at ~360 nm corresponded to the absorption of titanium–oxo clusters, and the adsorption band edges at ~480 nm corresponded to the absorption of functional amine. When NH_2-MIL-125(Ti) was converted to TiO_2@NH_2-MIL-125(Ti) nanocomposites, the absorption intensity of titanium–oxo clusters increased, while the absorption intensity of functional amine decreased for MT-0.5, MT-1, and MT-2. Furthermore, the absorption intensity of the functional amine nearly disappeared for NH_2-MIL-125(Ti) derived TiO_2 due to the ligand loss, and the absorption of titanium–oxo clusters was maximized due to the good crystallization of anatase TiO_2.

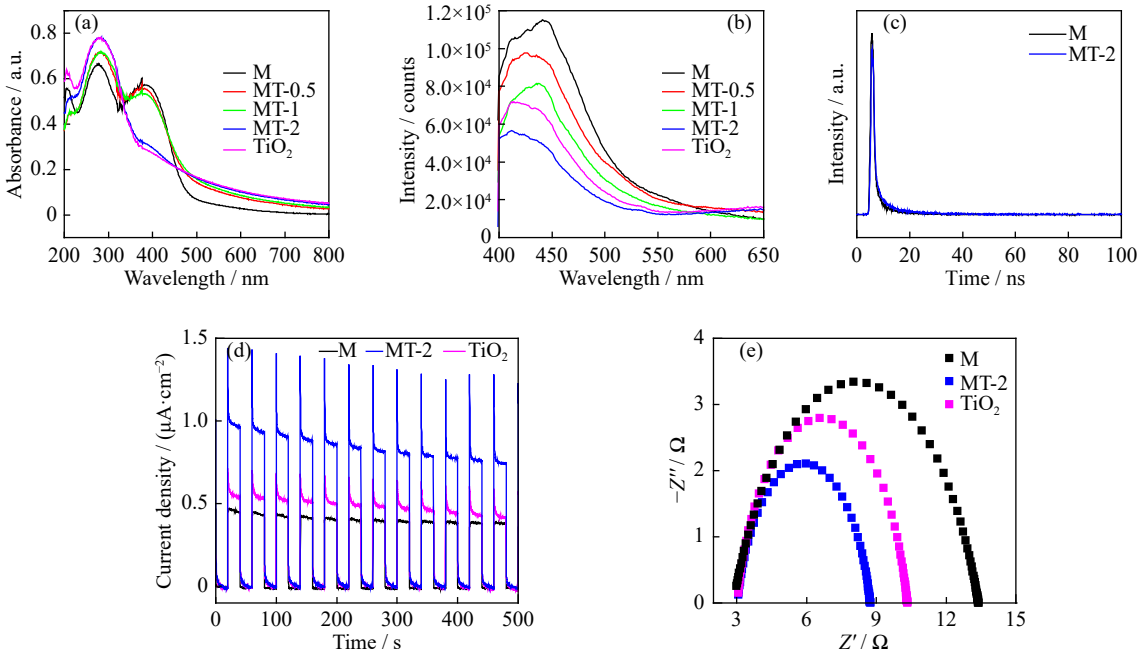

Fig. 6. (a) UV–Vis DRS spectra and (b) photoluminescence spectra of NH_2-MIL-125, TiO_2@NH_2-MIL-125, and TiO_2; (c) time-resolution photoluminescence of M and MT-2; (d) transient photocurrent density and (e) Nyquist spectra of NH_2-MIL-125, TiO_2@NH_2-MIL-125, and TiO_2.

Fig. 6(b) shows the steady state photoluminescence (PL) emission spectroscopy of as-prepared samples. NH_2-MIL-125(Ti) had the strongest PL emission signal, while a series of decreased peaks can be observed for TiO_2@NH_2-MIL-125(Ti) nanocomposites. Further, MT-2 exhibited the weakest signal among all the samples, which indicated that the recombination of electron–hole pairs was drastically suppressed. The time-resolution photoluminescence (TRPL) decay spectra and the corresponding average lifetimes of M and MT-2 are shown in Fig. 6(c) and Table S4, respectively. MT-2 had an average lifetime of 3.54 ns, which was much longer than that of M (2.15 ns). A longer fluorescent lifetime implies lower charge recombination rate, and thus higher photocatalytic activity.

Photoelectrochemical experiments were made to investigate the photogeneration and transfer of carriers under simulated solar irradiation. The transient photocurrent response of M, MT-2, and TiO_2 was recorded for several on-off cycles. As shown in Fig. 6(d), the photocurrent density increased drastically for MT-2 compared with M. When TiO_2@NH_2-MIL-125(Ti) converted completely to TiO_2, the photocurrent density decreased significantly. Eelectrochemical impedance curves were measured (Fig. 6(e)) to investigate the charge transfer resistance. Obviously, MT-2 had a smaller radius of Nyquist circle compared with M, indicating smaller charge transfer resistance and faster carriers transfer rate. The results demonstrated that MT-2 exhibited the highest carriers' transfer and separation efficiency compared with M and M derived TiO_2.

Based on the discussions, the as-synthesized TiO_2@NH_2-MIL-125 nanocomposites have many advantages for photocatalytic Cr(VI) reduction. Firstly, the mesoporous structure of NH_2-MIL-125 derived TiO_2@NH_2-MIL-125 nanocomposite can efficiently accelerate mass/charge transfer, and thus improve the conductivity of photocatalyst. The result was further proved by the contact angle measurements (Fig. S5). The contact angles were 59.14° for M and 12.81° for MT-2. The lower contact angle for MT-2 indicates the higher hydrophilicity, which can facilitate the mass/charge transfer during the photocatalytic degradation of Cr(VI) reduction reaction. Secondly, the unsaturated titanium–oxo cluster provides more active sites, improving the adsorption

of reactant and surface photoredox reaction. Lastly, the intimate interface between the two components can accelerate the separation and transport of carriers. Therefore, TiO_2@NH_2-MIL-125 nanocomposite would be a promising photocatalyst for Cr(VI) reduction.

3.3. Photocatalytic degradation of Cr(VI)

TiO_2@NH_2-MIL-125 nanocomposites were applied to photocatalytic degradation of aqueous Cr(VI) solution under pH of 6, which was made of $K_2Cr_2O_7$ dissolved into distilled water. As shown in Fig. 7(a), all the TiO_2@NH_2-MIL-125(Ti) nanocomposites (MT-0.5, MT-1, MT-2) displayed better photocatalytic performance than NH_2-MIL-125 (M) under 300 W of Xe lamp irradiation. Typically, MT-2 demonstrated the highest photocatalytic degradation efficiency among all the samples, and Cr(VI) was removed nearly 100% within 40 min. Comparably, NH_2-MIL-125 (M), MT-0.5, MT-1, and NH_2-MIL-125 derived TiO_2 depicted ~20%, ~48%, ~77%, and ~87% removal efficiency within 40 min. Correspondingly, the apparent reaction rate constant (k) was calculated by the pseudo-first order model according to the equation $\ln(C_t/C_0) = -kt$, where C_0 is the original concentration of Cr(VI), and C_t is the concentration of Cr(VI) at time t. The rate constants for all the samples followed the order that MT-2 > TiO_2 > MT-1 > MT-0.5 > M, further confirming the highest photocatalytic reaction rate of MT-2 (Fig. 7(b)). Furthermore, the surface state and composition of the used photocatalyst (MT-2 as representative) after the photocatalytic Cr(VI) reduction reaction were investigated via XPS. As shown in Fig. S6(a), Cr element can be observed in the survey spectra of the used MT-2 except C, N, O, and Ti. As shown in the high resolution XPS spectrum of Cr (Fig. S6(b)), the binding energies at ~587.2 and ~577.3 eV corresponded to Cr^{3+} $2p_{1/2}$ and Cr^{3+} $2p_{3/2}$. The results indicated that all of the toxic Cr(VI) has been converted to Cr(III) through the photocatalytic reduction reaction [60].

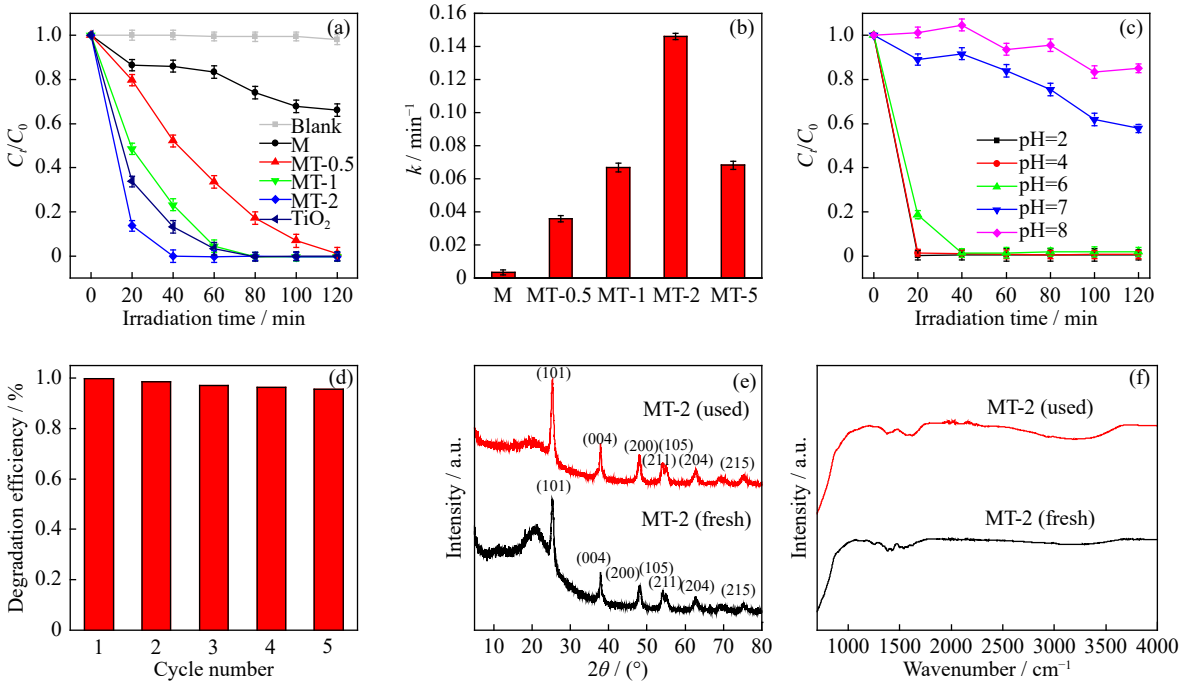

Fig. 7. (a) Photocatalytic Cr(VI) reduction curves and (b) the corresponding rate constants k over NH_2-MIL-125, TiO_2@NH_2-MIL-125 nanocomposites, and TiO_2; (c) photocatalytic Cr(VI) reduction curves at different pH with MT-2 as photocatalyst; (d) cyclic experiments of photocatalytic Cr(VI) reaction over MT-2; (e) XRD patterns and (f) FTIR spectra of MT-2 before and after Cr(VI) reduction experiments.

The pH of Cr(VI) aqueous solution is also a critical factor that determining Cr(VI) reduction efficiency in practical applications of photocatalysts. Taken MT-2 as example, the initial pH of the Cr(VI) solution was adjusted at 2, 4, 6, 7, or 8 to investigate the photocatalytic Cr(VI) reduction performance. As displayed in Fig. 7(c), Cr(VI) can be nearly removed within 20 min at pH of 2 and 3, and removed completely within 40 min at pH of 6. The reason is that lower pH is thermodynamically conducive to the reduction of Cr(VI) [61]. When pH was increased to 7 or 8, the degradation efficiency remarkably deteriorated because of the forming of $Cr(OH)_3$ precipitate, which adhered to the active site of the catalyst and hindered the photocatalytic reaction [62].

Stability and reusability are also determinative factors for photocatalysts in practical applications, and MT-2 was selected as representative for the stability tests. The long-term stability of MT-2 in photocatalytic Cr(VI) reduction was investigated via cycling experiments and is shown in Fig. 7(d). Obviously, no apparent deterioration of photodegradation efficiency can be observed after 5 cycles, demonstrating excellent stability of MT-2. The XRD patterns (Fig. 7(e)) and FTIR spectra (Fig. 7(f)) of the used MT-2 were similar to those of the unused photocatalyst, indicating that the crystalline structure and composition of the photocatalyst also re-

mained intact. Moreover, the SEM image shown in Fig. S7 indicated that the morphology of used photocatalyst was well retained. The results indicated the excellent reusability and stability of the TiO_2@NH_2-MIL-125 nanocomposite photocatalyst.

Further, high-pressure xenon lamp assigned with band-pass filters with central wavelengths of 365, 400, and 500 nm was used as light source to evaluate the photocatalytic performance of MT-2 and the results are shown in Fig. S8(a). It can be seen that Cr(VI) was nearly removed completely after 100 min over high-pressure with filters of 365 nm. Comparably, Cr(VI) was nearly removed completely after 2 h for MT-2 with filters of 400 nm and was removed ~80% after 2 h for MT-2 with filters of 500 nm. The apparent reaction rate constants (k) were calculated and are shown in Fig. S8(b), indicating the rate constant for MT-2 decreased with the increase of central wavelength for band-pass filters. Thus, it can be concluded that the MT-2 demonstrated rather excellent photocatalytic performance when the wavelength of photon increased to 400 and 500 nm, illustrating the photocatalyst has excellent photocatalytic performance over a broad solar spectrum.

MT-2 was also used for photocatalytic degradation of methylene blue (MB) under the same irradiation. The degradation curve is shown in Fig. S9 and ~25% MB was degraded after 3 h irradiation.

3.4. Possible photocatalytic mechanism

The electronic structures of NH_2-MIL-125 and NH_2-MIL-125 derived TiO_2 were investigated via Mott-Schottky measurements. As shown in Fig. 8(a), the n-type semiconductor feature could be observed, and the flat band potentials (E_{fb}) determined from the x-axis intercepts of the liner region were −0.70 V vs. Ag/AgCl and −0.56 V vs. Ag/AgCl for M and TiO_2 (equivalent to −0.50 vs. NHE and −0.36 V vs. NHE). The flat band potential is more positive by approximately ~0.1 V than the bottom of the conduction band for n-type semiconductors [63]. Therefore, the LUMO of M and the CBM of TiO_2 could be regarded as −0.60 V vs. NHE and −0.46 V vs. NHE. Based on the plots of $(ahv)^2$ versus hv (Fig. 8(b)), where a, h, and v represent the adsorption coefficient, Planks constant, and incident photon frequency, the bandgap energies of M and TiO_2 were ~2.70 eV and ~3.24 eV. Combined with the bandgaps of M and TiO_2, the HOMO of M and VBM of TiO_2 could be estimated to be +2.1 V and +2.78 V vs. NHE according to $E_{VB} = E_{CB} + E_g$, where E_g is the band gap energy, E_{VB} is the valence band (VB) potential, and E_{CB} is the conduction band (CB) potential. The calculated VBM and HOMO of TiO_2 and M can also be verified by the valence band XPS (Fig. S10) [64].

Additionally, the carrier densities (N_d) of M, MT-2, and NH_2-MIL-125 derived TiO_2 were calculated based on Mott-

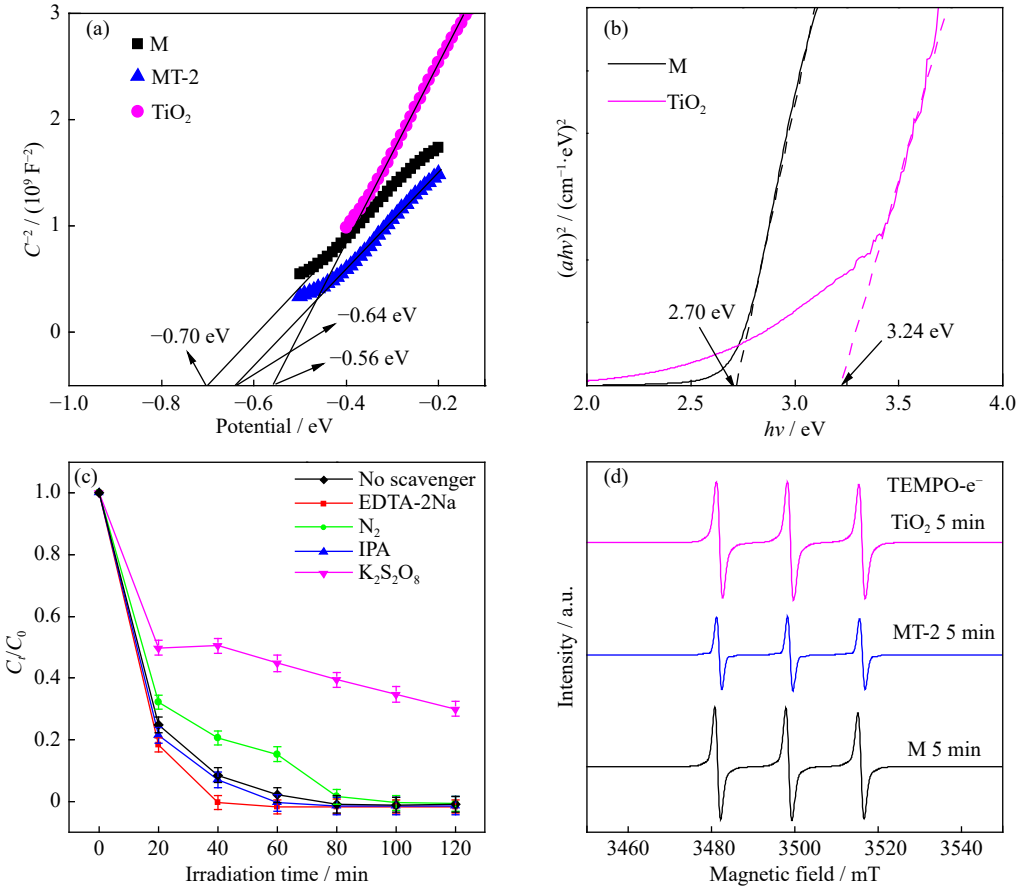

Fig. 8. (a) Mott-Schottky curves at 1000 Hz of M, MT-2, and TiO_2 (C is the capacitance of the space charge region); (b) band gaps of M and TiO_2; (c) effect of different scavengers on Cr(VI) reduction; (d) EPR spectra of e^- trapped by TEMPO over M, MT-2, and TiO_2.

Schottky plots and the results are shown in Table S5 [65]. The N_d values were 1.65×10^{22}, 2.36×10^{20}, and 1.48×10^{20} cm^{-3} for M, MT-2, and TiO_2. MT-2 had a higher N_d value compared with TiO_2, whichis contributed to higher photocatalytic performance. It's worth mentioning that M had a higher N_d value than MT-2, but the higher carrier density for M did not lead to improved photocatalytic performance because of the limited transfer and separation efficiency of carriers.

In order to investigate the active species produced in the photocatalytic reaction, a series of free-radical trapping experiments were performed. The scavengers including ethylene diamine tetraacetic acid disodium salt (EDTA-2Na), N_2, isopropanol (IPA), and potassium peroxydisulfate ($K_2S_2O_8$) were employed to quench the holes (h^+), superoxide radials ($\cdot O_2^-$), hydroxyl radicals ($\cdot$OH), and electrons (e^-) generated in the photocatalytic reaction. As depicted in Fig. 8(c), the photocatalytic Cr(VI) reduction efficiency over MT-2 was suppressed to ~50% within 40 min with the addition of $K_2S_2O_8$ (e^-). It can be inferred that e^- are the chief carriers in the process of Cr(VI) reduction reaction. Meanwhile, the photocatalytic efficiency was slightly suppressed with the addition of N_2 ($\cdot O_2^-$), indicating $\cdot O_2^-$ which formed via reaction between electrons and O_2 molecules absorbed on the surface of photocatalyst can also be an important radical in photocatalytic Cr(VI) reduction reaction. The result could further convince that e^- is the upmost active radical in Cr(VI) reduction reaction. The photocatalytic efficiency has no apparent changes with the addition of IPA ($\cdot$OH), indicating $\cdot$OH is not the chief species in photocatalytic reaction. Unusually, photocatalytic Cr(VI) reduction efficiency was enhanced slightly with the introduction of EDTA-2Na (h^+). The reason can be explained that EDTA-2Na would capture photogenerated holes, which can suppress the recombination of photogenerated carriers, and then permit more free electrons participating in the Cr(VI) reduction reaction.

Additionally, the EPR spin-trap measurements were conducted to validate the active species. The 2,2,6,6-tetramethylpiperidine-1-oxyl (TEMPO)-e^- measurements for M, MT-2, and MT derived TiO_2 under the irradiation for 5 min are shown in Fig. 8(d) and triplet EPR spectrum with intensity of 1:1:1 can be observed. MT-2 had the weaker TEMPO-e^- signal compared with M and TiO_2, indicating improved photogenerated electrons in the photocatalytic process. Also, 5,5-dimethyl-1-pyrrolidine-N-oxide (DMPO)-$\cdot O_2^-$ measurements were employed and are shown in Fig. S11. Four typical signals of DMPO-$\cdot O_2^-$ can be detected upon irradiation for 5 min. Notably, the DMPO-$\cdot O_2^-$ signal for MT-2 was much stronger than those of M and TiO_2. The results agree well with the best photocatalytic performance of MT-2.

According to the band alignments of TiO_2 and NH_2-MIL-125(Ti) as well as the radical generation results, the type-II photocatalytic Cr(VI) reduction scheme was proposed (Fig. 9). The schematic bandgap of TiO_2@NH_2-MIL-125(Ti) nanocomposites is shown in Fig. 9(a). When irradiated with Xe lamp, photogenerated electrons transfer from the organic linker of NH_2-MIL-125(Ti) to the titanium–oxo cluster, leaving the holes in the organic ligand. TiO_2 generates electron–holes pairs in the CB and VB respectively. Further, the photoinduced electrons in the LUMO of NH_2-MIL-125 are apt to migrate from the LUMO of NH_2-MIL-125 to the CB of TiO_2 driven by the potential difference, and photogenerated holes in the VB of TiO_2 migrate to the HOMO of NH_2-MIL-125. The transfer route of photogenerated electron–holes leads to efficient separation of photogenerated electron–hole pairs in TiO_2@NH_2-MIL-125(Ti) composite. Consequently, the photogenerated electrons accumulated in the CB of TiO_2 can involve into the Cr(VI) reduction reaction. Also, because the potential of $O_2/\cdot O_2^-$ (−0.33 eV vs. NHE) is more positive than the CB of TiO_2, the electrons accumulated on the CB of TiO_2 react with the dissolved oxygen to generated $\cdot O_2^-$, which is thermodynamically feasible. Accordingly, photogenerated electrons and $\cdot O_2^-$ are both involved into the photocatalytic Cr(VI) reduction reaction.

In brief, the schematic diagram of reduction path of Cr(VI) ions can been depicted in Fig. 9(b). Firstly, Cr(VI) ions adsorb on the surface of photocatalyst, and then are reduced to Cr(III) by the photogenerated electrons and $\cdot O_2^-$ produced by TiO_2@NH_2-MIL-125(Ti) composite. Finally, the Cr(III) is desorbed for the surface of photocatalyst and released into the solution. TiO_2@NH_2-MIL-125 as a photocatalyst in Cr(VI) photoreduction provides efficient generation and separation of photogenerated electron–holes pairs, and thus achieves excellent photocatalytic performance.

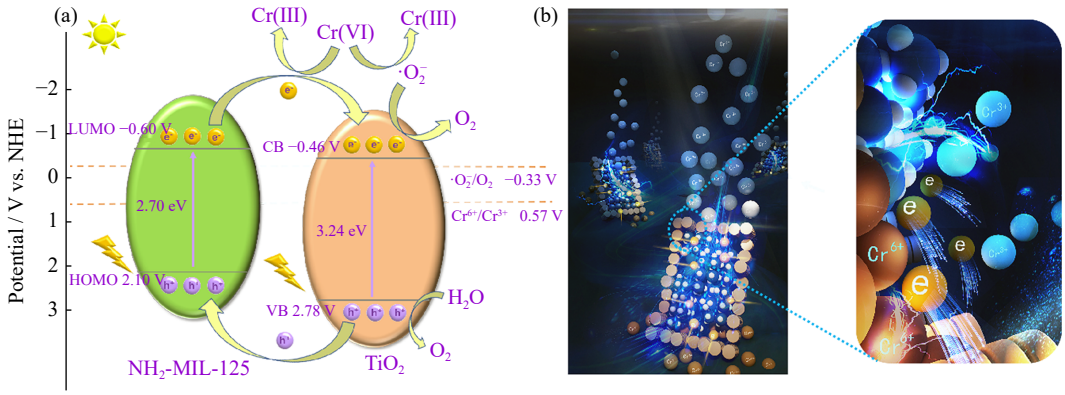

Fig. 9. (a) Schematic bandgap of TiO_2@NH_2-MIL-125(Ti) nanocomposites; (b) schematic diagram of photocatalytic reduction path of Cr(VI) ions.

4. Conclusion

In summary, we adopted a facile method to prepare TiO_2@NH_2-MIL-125(Ti) nanocomposites via an *in situ* distilled water-etched route using NH_2-MIL-125(Ti) as precursor. The prepared TiO_2@NH_2-MIL-125(Ti) nanocomposites have mesoporous structure and unsaturated Ti–O clusters, which endow them improved photocatalytic Cr(VI) degradation efficiency. Compared with NH_2-MIL-125(Ti) and NH_2-MIL-125(Ti) derived TiO_2, the optimized MT-2 exhibited superior Cr(VI) degradation efficiency and possessed good reusability and stability. Based on the structure and thermodynamic characteristics, the type-II scheme mechanism was speculated to boost the separation of photogenerated carriers and the formation of reactive species. This work proposes a promising and eco-friendly route for preparing TiO_2@NH_2-MIL-125(Ti) nanocomposites and opens up a new pathway for water remediation.

Acknowledgements

This work was financially supported by the National Natural Science Foundation of China (Nos. 61204078, 21671059, and 21877027), the Program for Innovative Research Team (in Science and Technology) of Henan Normal University (No. 2022TD03), the Henan Science and Technology Program (No. 21B150005), and the Scientific and Technological Innovation Team of Henan Normal University (No. 2022TD03). The authors would like to thank Yuxiang Wu from Shiyanjia Lab (www.shiyanjia.com) for the EPR measurements and analysis.

Conflict of Interest

The authors declare that there are no competing financial interests or personal relationships that could have appeared to influence the work reported in this paper.

Supplementary Information

The online version contains supplementary material available at https://doi.org/10.1007/s12613-022-2559-4.

References

[1] Y.X. Li, H. Fu, P. Wang, C. Zhao, W. Liu, and C.C. Wang, Porous tube-like ZnS derived from rod-like ZIF-L for photocatalytic Cr(VI) reduction and organic pollutants degradation, *Environ. Pollut.*, 256(2020), art. No. 113417.

[2] J. Geng, F. Gu, and J.M. Chang, Fabrication of magnetic lignosulfonate using ultrasonic-assisted *in situ* synthesis for efficient removal of Cr(VI) and Rhodamine B from wastewater, *J. Hazard. Mater.*, 375(2019), p. 174.

[3] W.J. Jiang, M. Pelaez, D.D. Dionysiou, M.H. Entezari, D. Tsoutsou, and K. O'Shea, Chromium(VI) removal by maghemite nanoparticles, *Chem. Eng. J.*, 222(2013), p. 527.

[4] C.E. Barrera-Díaz, V. Lugo-Lugo, and B. Bilyeu, A review of chemical, electrochemical and biological methods for aqueous Cr(VI) reduction, *J. Hazard. Mater.*, 223-224(2012), p. 1.

[5] S. Jamshidifard, S. Koushkbaghi, S. Hosseini, *et al*., Incorporation of UiO-66-NH2 MOF into the PAN/chitosan nanofibers for adsorption and membrane filtration of Pb(II), Cd(II) and Cr(VI) ions from aqueous solutions, *J. Hazard. Mater.*, 368(2019), p. 10.

[6] S. Wu, X.B. He, L.J. Wang, and K.C. Chou, High Cr(VI) adsorption capacity of rutile titania prepared by hydrolysis of $TiCl_4$ with $AlCl_3$ addition, *Int. J. Miner. Metall. Mater.*, 27(2020), No. 8, p. 1157.

[7] F. Chen, Q. Yang, Y.L. Wang, *et al*., Efficient construction of bismuth vanadate-based Z-scheme photocatalyst for simultaneous Cr(VI) reduction and ciprofloxacin oxidation under visible light: Kinetics, degradation pathways and mechanism, *Chem. Eng. J.*, 348(2018), p. 157.

[8] J.H. Qiu, X.F. Zhang, X.G. Zhang, *et al*., Constructing $Cd_{0.5}Zn_{0.5}S$@ZIF-8 nanocomposites through self-assembly strategy to enhance Cr(VI) photocatalytic reduction, *J. Hazard. Mater.*, 349(2018), p. 234.

[9] Z.P. Cheng, Q. Dong, S. Chen, *et al*., Novel $AgCl_xBr_{1-x}$ solid solutions photocatalyst with enhanced photocatalytic activity for reduction of Cr^{6+} and oxidation of Bisphenol A under simulated sunlight, *Mater. Res. Bull.*, 139(2021), art. No. 111257.

[10] F. Xu, H.M. Chen, C.Y. Xu, *et al*., Ultra-thin Bi_2WO_6 porous nanosheets with high lattice coherence for enhanced performance for photocatalytic reduction of Cr(VI), *J. Colloid Interface Sci.*, 525(2018), p. 97.

[11] H. Furukawa, K.E. Cordova, M. O'Keeffe, and O.M. Yaghi, The chemistry and applications of metal-organic frameworks, *Science*, 341(2013), No. 6149, art. No. 1230444.

[12] M.A. Syzgantseva, C.P. Ireland, F.M. Ebrahim, B. Smit, and O.A. Syzgantseva, Metal substitution as the method of modifying electronic structure of metal-organic frameworks, *J. Am. Chem. Soc.*, 141(2019), No. 15, p. 6271.

[13] T. Zhang and W.B. Lin, Metal-organic frameworks for artificial photosynthesis and photocatalysis, *Chem. Soc. Rev.*, 43(2014), No. 16, p. 5982.

[14] M.A. Nasalevich, M. van der Veen, F. Kapteijn, and J. Gascon, Metal-organic frameworks as heterogeneous photocatalysts: Advantages and challenges, *CrystEngComm*, 16(2014), No. 23, p. 4919.

[15] S. Naghdi, A. Cherevan, A. Giesriegl, *et al*., Selective ligand removal to improve accessibility of active sites in hierarchical MOFs for heterogeneous photocatalysis, *Nat. Commun.*, 13(2022), art. No. 282.

[16] A. Corma, H. García, and F.X.L. i Xamena, Engineering metal organic frameworks for heterogeneous catalysis, *Chem. Rev.*, 110(2010), No. 8, p. 4606.

[17] H.Q. Xu, J.H. Hu, D.K. Wang, *et al*., Visible-light photoreduction of CO_2 in a metal-organic framework: Boosting electron–hole separation via electron trap states, *J. Am. Chem. Soc.*, 137(2015), No. 42, p. 13440.

[18] X.L. Chen, S.N. Xiao, H. Wang, *et al*., MOFs conferred with transient metal centers for enhanced photocatalytic activity, *Angew. Chem. Int. Ed.*, 59(2020), No. 39, p. 17182.

[19] X. Wang, X.L. Zhang, W. Zhou, L.Q. Liu, J.H. Ye, and D.F. Wang, An ultrathin porphyrin-based metal-organic framework for efficient photocatalytic hydrogen evolution under visible light, *Nano Energy*, 62(2019), p. 250.

[20] J. Wang, A.S. Cherevan, C. Hannecart, *et al*., Ti-based MOFs: New insights on the impact of ligand composition and hole scavengers on stability, charge separation and photocatalytic hydrogen evolution, *Appl. Catal. B*, 283(2021), art. No. 119626.

[21] S.H. Wu, X.F. Xing, D. Wang, *et al*., Highly ordered hierarchically macroporous MIL-125 with high specific surface area for photocatalytic CO_2 fixation, *ACS Sustainable Chem. Eng.*, 8(2020), No. 1, p. 148.

[22] Y.X. Li, C.C. Wang, H.F. Fu, and P. Wang, Marigold-flower-like TiO_2/MIL-125 core–shell composite for enhanced photocatalytic Cr(VI) reduction, *J. Environ. Chem. Eng.*, 9(2021), No. 4, art. No. 105451.
[23] L. Li, X.S. Wang, T.F. Liu, and J.H. Ye, Titanium-based MOF materials: From crystal engineering to photocatalysis, *Small Methods*, 4(2020), No. 12, art. No. 2000486.
[24] G. Wen and Z.G. Guo, Facile modification of NH_2-MIL-125(Ti) to enhance water stability for efficient adsorptive removal of crystal violet from aqueous solution, *Colloids Surf. A*, 541(2018), p. 58.
[25] S. Hu, M. Liu, K.Y. Li, *et al*., Solvothermal synthesis of NH_2-MIL-125(Ti) from circular plate to octahedron, *CrystEngComm*, 16(2014), No. 41, p. 9645.
[26] F. Guo, J.H. Guo, P. Wang, *et al*., Facet-dependent photocatalytic hydrogen production of metal-organic framework NH_2-MIL-125(Ti), *Chem. Sci.*, 10(2019), No. 18, p. 4834.
[27] G. Capano, F. Ambrosio, S. Kampouri, K.C. Stylianou, A. Pasquarello, and B. Smit, On the electronic and optical properties of metal-organic frameworks: Case study of MIL-125 and MIL-125-NH_2, *J. Phys. Chem. C*, 124(2020), No. 7, p. 4065.
[28] X.M. Cheng, X.Y. Dao, S.Q. Wang, J. Zhao, and W.Y. Sun, Enhanced photocatalytic CO_2 reduction activity over NH_2-MIL-125(Ti) by facet regulation, *ACS Catal.*, 11(2021), No. 2, p. 650.
[29] S. Gao, W.L. Cen, Q. Li, *et al*., A mild one-step method for enhancing optical absorption of amine-functionalized metal-organic frameworks, *Appl. Catal. B*, 227(2018), p. 190.
[30] F. Mohammadnezhad, S. Kampouri, S.K. Wolff, *et al*., Tuning the optoelectronic properties of hybrid functionalized MIL-125-NH_2 for photocatalytic hydrogen evolution, *ACS Appl. Mater. Interfaces*, 13(2021), No. 4, p. 5044.
[31] S. Kampouri, T.N. Nguyen, M. Spodaryk, *et al*., Concurrent photocatalytic hydrogen generation and dye degradation using MIL-125-NH2 under visible light irradiation, *Adv. Funct. Mater.*, 28(2018), No. 52, art. No. 1806368.
[32] Y.W. Sun, Y. Liu, J. Caro, X.W. Guo, C.S. Song, and Y. Liu, In-plane epitaxial growth of highly *c*-oriented NH_2-MIL-125(Ti) membranes with superior H_2/CO_2 selectivity, *Angew. Chem. Int. Ed.*, 57(2018), No. 49, p. 16088.
[33] J.H. Qiu, M. Li, H.T. Wang, and J.F. Yao, Integration of plasmonic effect into MIL-125-NH_2: An ultra-efficient photocatalyst for simultaneous removal of ternary system pollutants, *Chemosphere*, 242(2020), art. No. 125197.
[34] V. Muelas-Ramos, C. Belver, J.J. Rodriguez, and J. Bedia, Synthesis of noble metal-decorated NH_2-MIL-125 titanium MOF for the photocatalytic degradation of acetaminophen under solar irradiation, *Sep. Purif. Technol.*, 272(2021), art. No. 118896.
[35] Y.C. Zhou, P. Wang, H.F. Fu, C. Zhao, and C.C. Wang, Ternary Ag/Ag_3PO_4/MIL-125-NH_2 Z-scheme heterojunction for boosted photocatalytic Cr(VI) cleanup under visible light, *Chin. Chem. Lett.*, 31(2020), No. 10, p. 2645.
[36] S.Y. Zhang, M. Du, Z.P. Xing, Z.Z. Li, K. Pan, and W. Zhou, Defect-rich and electron-rich mesoporous Ti-MOFs based NH_2-MIL-125(Ti)@$ZnIn_2S_4$/CdS hierarchical tandem heterojunctions with improved charge separation and enhanced solar-driven photocatalytic performance, *Appl. Catal. B*, 262(2020), art. No. 118202.
[37] H. Wang, Q. Zhang, J.J. Li, *et al*., The covalent Coordination-driven Bi_2S_3@NH_2-MIL-125(Ti)-SH heterojunction with boosting photocatalytic CO_2 reduction and dye degradation performance, *J. Colloid Interface Sci.*, 606(2022), p. 1745.
[38] J. Chen, M.G. Wang, J. Han, and R. Guo, TiO_2 nanosheet/NiO nanorod hierarchical nanostructures: p-n heterojunctions towards efficient photocatalysis, *J. Colloid Interface Sci.*, 562(2020), p. 313.
[39] G.Q. Zhang, X. Yang, C.X. He, P.X. Zhang, and H.W. Mi, Constructing a tunable defect structure in TiO_2 for photocatalytic nitrogen fixation, *J. Mater. Chem. A*, 8(2020), No. 1, p. 334.
[40] X.G. Han, Q. Kuang, M.S. Jin, Z.X. Xie, and L.S. Zheng, Synthesis of titania nanosheets with a high percentage of exposed (001) facets and related photocatalytic properties, *J. Am. Chem. Soc.*, 131(2009), No. 9, p. 3152.
[41] J.F. Chen, X.D. Zhang, F.K. Bi, X.L. Zhang, Y. Yang, and Y.X. Wang, A facile synthesis for uniform tablet-like TiO_2/C derived from Materials of Institut Lavoisier-125(Ti) (MIL-125(Ti)) and their enhanced visible light-driven photodegradation of tetracycline, *J. Colloid Interface Sci.*, 571(2020), p. 275.
[42] L.F. Liu, F.Y. Zhang, J.L. Zhang, *et al*., Interfacial assembly and hydrolysis for synthesizing a TiO_2/metal-organic framework composite, *Soft Matter*, 13(2017), No. 48, p. 9174.
[43] Y. Zhang, Z.Y. Zhao, J.R. Chen, *et al*., C-doped hollow TiO_2 spheres: *In situ* synthesis, controlled shell thickness, and superior visible-light photocatalytic activity, *Appl. Catal. B*, 165(2015), p. 715.
[44] H. Lee, H.S. Jang, N.Y. Kim, and J.B. Joo, Cu-doped TiO_2 hollow nanostructures for the enhanced photocatalysis under visible light conditions, *J. Ind. Eng. Chem.*, 99(2021), p. 352.
[45] Q.Q. Liu, J.X. Huang, H. Tang, X.H. Yu, and J. Shen, Construction 0D TiO_2 nanoparticles/2D CoP nanosheets heterojunctions for enhanced photocatalytic H_2 evolution activity, *J. Mater. Sci. Technol.*, 56(2020), p. 196.
[46] L.L. Wang, G.G. Tang, S. Liu, *et al*., Interfacial active-site-rich 0D Co_3O_4/1D TiO_2 p-n heterojunction for enhanced photocatalytic hydrogen evolution, *Chem. Eng. J.*, 428(2022), art. No. 131338.
[47] J. Shen, R. Wang, Q.Q. Liu, X.F. Yang, H. Tang, and J. Yang, Accelerating photocatalytic hydrogen evolution and pollutant degradation by coupling organic co-catalysts with TiO_2, *Chin. J. Catal.*, 40(2019), No. 3, p. 380.
[48] X.Y. Li, Y.H. Pi, Q.Q. Hou, *et al*., Amorphous TiO_2@NH_2-MIL-125(Ti) homologous MOF-encapsulated heterostructures with enhanced photocatalytic activity, *Chem. Commun.*, 54(2018), No. 15, p. 1917.
[49] J.M. Hu, J. Ding, and Q. Zhong, *In situ* fabrication of amorphous TiO_2/NH_2-MIL-125(Ti) for enhanced photocatalytic CO_2 into CH_4 with H_2O under visible-light irradiation, *J. Colloid Interface Sci.*, 560(2020), p. 857.
[50] B.X. Zhang, J.L. Zhang, X.N. Tan, *et al*., MIL-125-NH_2@TiO_2 core–shell particles produced by a post-solvothermal route for high-performance photocatalytic H_2 production, *ACS Appl. Mater. Interfaces*, 10(2018), No. 19, p. 16418.
[51] R. Bibi, H.L. Huang, M. Kalulu, *et al*., Synthesis of amino-functionalized Ti-MOF derived yolk-shell and hollow heterostructures for enhanced photocatalytic hydrogen production under visible light, *ACS Sustainable Chem. Eng.*, 7(2019), No. 5, p. 4868.
[52] M. Zhang, J.N. Chang, Y.F. Chen, *et al*., Controllable synthesis of COFs-based multicomponent nanocomposites from core–shell to yolk-shell and hollow-sphere structure for artificial photosynthesis, *Adv. Mater.*, 33(2021), No. 48, art. No. 2105002.
[53] L.M. Sun, Y.S. Yuan, F. Wang, Y.L. Zhao, W.W. Zhan, and X.G. Han, Selective wet-chemical etching to create TiO_2@MOF frame heterostructure for efficient photocatalytic hydrogen evolution, *Nano Energy*, 74(2020), p. 104909.
[54] X.M. Cheng, Y.M. Gu, X.Y. Zhang, *et al*., Crystallographic facet heterojunction of MIL-125-NH_2(Ti) for carbon dioxide photoreduction, *Appl. Catal. B*, 298(2021), art. No. 120524.
[55] M.A. Nasalevich, M.G. Goesten, T.J. Savenije, F. Kapteijn, and J. Gascon, Enhancing optical absorption of metal-organic frameworks for improved visible light photocatalysis, *Chem. Commun.*, 49(2013), No. 90, p. 10575.
[56] J.G. Yu, J.X. Low, W. Xiao, P. Zhou, and M. Jaroniec, En-

hanced photocatalytic CO_2-reduction activity of anatase TiO_2 by coexposed {001} and {101} facets, *J. Am. Chem. Soc.*, 136(2014), No. 25, p. 8839.

[57] D.L. Dai, J.H. Qiu, L. Zhang, H. Ma, and J.F. Yao, Amino-functionalized Ti-metal-organic framework decorated BiOI sphere for simultaneous elimination of Cr(VI) and tetracycline, *J. Colloid Interface Sci.*, 607(2022), p. 933.

[58] Z.Q. He, J.T. Tang, J. Shen, J.M. Chen, and S. Song, Enhancement of photocatalytic reduction of CO_2 to CH_4 over TiO_2 nanosheets by modifying with sulfuric acid, *Appl. Surf. Sci.*, 364(2016), p. 416.

[59] P. Karthik, E. Balaraman, and B. Neppolian, Efficient solar light-driven H_2 production: Post-synthetic encapsulation of a Cu_2O co-catalyst in a metal-organic framework (MOF) for boosting the effective charge carrier separation, *Catal. Sci. Technol.*, 8(2018), No. 13, p. 3286.

[60] X.S. Wang, C.H. Chen, F. Ichihara, *et al.*, Integration of adsorption and photosensitivity capabilities into a cationic multivariate metal-organic framework for enhanced visible-light photoreduction reaction, *Appl. Catal. B*, 253(2019), p. 323.

[61] Y.J. Fu, K.J. Zhang, Y. Zhang, Y.Q. Cong, and Q. Wang, Fabrication of visible-light-active MR/NH_2-MIL-125(Ti) homojunction with boosted photocatalytic performance, *Chem. Eng. J.*, 412(2021), art. No. 128722.

[62] V. Chevalier, J. Martin, D. Peralta, A. Roussey, and F. Tardif, Performance of HKUST-1 metal-organic framework for a VOCs mixture adsorption at realistic concentrations ranging from 0.5 to 2.5 ppmv under different humidity conditions, *J. Environ. Chem. Eng.*, 7(2019), No. 3, art. No. 103131.

[63] A. Ishikawa, T. Takata, J.N. Kondo, M. Hara, H. Kobayashi, and K. Domen, Oxysulfide $Sm_2Ti_2S_2O_5$ as a stable photocatalyst for water oxidation and reduction under visible light irradiation ($\lambda \leq 650$ nm), *J. Am. Chem. Soc.*, 124(2002), No. 45, p. 13547.

[64] S. Wu, H.T. Yu, S. Chen, and X. Quan, Enhanced photocatalytic H_2O_2 production over carbon nitride by doping and defect engineering, *ACS Catal.*, 10(2020), No. 24, p. 14380.

[65] W.C. Cui, J.P. Shang, H.Y. Bai, *et al.*, *In-situ* implantation of plasmonic Ag into metal-organic frameworks for constructing efficient Ag/NH_2-MIL-125/TiO_2 photoanode, *Chem. Eng. J.*, 388(2020), art. No. 124206.